npj | climate and atmospheric science

Article

Published in partnership with CECCR at King Abdulaziz University

https://doi.org/10.1038/s41612-024-00864-2

Irreversibility of winter precipitation over the Northeastern Pacific and Western North America against CO_2 forcing

Zhenhao Xu[1,2,3], Yu Kosaka[2] ✉, Masaki Toda[2,4], Tomoki Iwakiri[5,6], Gang Huang[1,3] ✉, Fei Ji[7,8], Ayumu Miyamoto[2,9] & Weichen Tao[1]

Comprehending the resilience of regional hydroclimate in response to CO_2 removal is essential for guiding future mitigation and adaptation strategies. Using an ensemble of model simulations forced by idealized CO_2 ramp-up followed by ramp-down, here we show that the winter precipitation over the Northeastern Pacific and Western North America (NPWNA) is irreversible even if global warming is reversed back to 2 °C level. This asymmetric change features a tripolar pattern and is tied to Aleutian Low intensification, which is driven by both zonal and meridional gradients of sea surface temperature (SST) anomalies in the tropical central-eastern Pacific. Distinct from the zonal SST gradient—explained by different timescales of surface and subsurface warming and ocean dynamical processes, amplified through the Bjerknes feedback—the meridional SST gradient originates from the southward shift of the intertropical convergence zone, maintained by the wind-evaporation-SST feedback. Our findings suggest that the regional hydrological risks over the NPWNA induced by CO_2 ramp-up cannot be fully eliminated by CO_2 removal even if the global warming level is restored back.

The unbridled anthropogenic CO_2 emission has already resulted in unprecedented rapid global warming, posing more and more severe climate risks to human society[1–4]. It is reported that in May 2023, an atmospheric CO_2 concentration measured at Mauna Loa Atmospheric Baseline Observatory hit 424 ppm, which has not been seen over the past 2 million years[3]. Meanwhile, 2023 also became the hottest year on record[5], when the global mean surface temperature (GMST) reached an increase of 1.34–1.54 °C above the preindustrial level[6]. Furthermore, future climate projections[7] in the Coupled Model Intercomparison Projects Phase 6 (CMIP6)[8] suggested that the 2 °C warming target proposed by the 2015 Paris Agreement[9] will not be attainable unless we can achieve net negative emissions, i.e., artificial reduction of atmospheric CO_2 concentration, in at least the second half of this century[10–13].

It is widely concerned that in case we indeed pass the 2 °C warming threshold, whether and to what extent can the earth's climate still be reversed by the carbon dioxide removal (CDR) method[14,15], as one of the geoengineering categories[16,17]. Generally, the so-called climate hysteresis or irreversibility is defined by comparing two climate states with the same atmospheric CO_2 concentration or global warming level[18]. By now, great efforts have been made to investigate and measure the hysteresis behaviors of several critical components in the climate system, including but not limited to the surface temperature[19–23], hydrological cycle[20,24–29], atmospheric meridional circulation[30,31], intertropical convergence zone (ITCZ)[18,32], monsoon system[33–36], Atlantic meridional overturning circulation (AMOC)[22,30,37,38], El Niño-Southern Oscillation (ENSO)[32,39,40], and mid-latitude storm tracks[41]. Among them, one of the most basic and important consensuses is that, in a symmetric changing CO_2 pathway with ramp-up followed by ramp-down, the same global warming level (e.g., 2 °C) can be achieved during the CO_2 ramp-down, but a lower concentration is required[22,23,27,28], due to the long-term memory of deep ocean, which slowly releases the accumulated heat on centennial timescales[42]. However, it is still unclear whether and how the regional hydroclimate, which are critical for local agriculture and human livelihoods, is irreversible.

To address the scientific questions above, we examine an idealized 5-member ensemble experiment using the Model for Interdisciplinary Research on Climate version 6 (MIROC6)[43,44] forced by CO_2 ramp-up

[1]State Key Laboratory of Numerical Modeling for Atmospheric Sciences and Geophysical Fluid Dynamics, Institute of Atmospheric Physics, Chinese Academy of Sciences, Beijing, China. [2]Research Center for Advanced Science and Technology, The University of Tokyo, Tokyo, Japan. [3]University of Chinese Academy of Sciences, Beijing, China. [4]Max-Planck Institute for Meteorology, Hamburg, Germany. [5]Atmosphere and Ocean Research Institute, The University of Tokyo, Chiba, Japan. [6]Meteorological Research Institute, Ibaraki, Japan. [7]College of Atmospheric Sciences, Lanzhou University, Lanzhou, China. [8]Collaborative Innovation Center for Western Ecological Safety, Lanzhou University, Lanzhou, China. [9]Scripps Institution of Oceanography, University of California, San Diego, La Jolla, CA, USA. ✉e-mail: ykosaka@atmos.rcast.u-tokyo.ac.jp; hg@mail.iap.ac.cn

followed by ramp-down (hereafter the CDR scenario), as per the protocols of the CDR Model Intercomparison Project (CDRMIP)[45] in CMIP6 (see Methods). We located two 20-year-long windows, called Windows 1 and 2, based on the ensemble empirical mode decomposition (EEMD) method (see Methods), to represent the climatology of the 2 °C global warming level during the ramp-up and ramp-down periods, respectively (Fig. 1a). Inspired by asymmetric response of the geopotential height at 500 hPa in boreal winter (December-January-February; DJF), which is characterized by wavetrain teleconnection (Fig. 1b), we investigate the irreversibility of the winter precipitation over the Northeastern Pacific and Western North America (NPWNA) and its potential driving mechanisms. To avoid any ambiguity, we note that the terms "irreversibility", "asymmetric response/change", and "hysteresis" used in the current study refer to the climatology difference between Windows 2 and 1 during boreal winter.

Results

Irreversibility of winter precipitation over the NPWNA

Hysteresis of 500 hPa geopotential height exhibits a wavetrain pattern reminiscent of the ENSO teleconnection[46] (Fig. 1b), hinting at an irreversible change in hydroclimate over the NPWNA region. As shown in Fig. 2a, b, the precipitation change in the NPWNA during boreal winter displays a "wetter-drier-wetter" tripolar structure. It suggests that during the ramp-down period, despite global warming level being the same, the region surrounding Seattle is drier, while the Gulf of Alaska and a California region with a remarkable westward extension until the dateline are wetter compared to the ramp-up period. Such an asymmetric response exceeds 10% magnitude of the climatology (Fig. 2c). The asymmetry is clear in anomaly

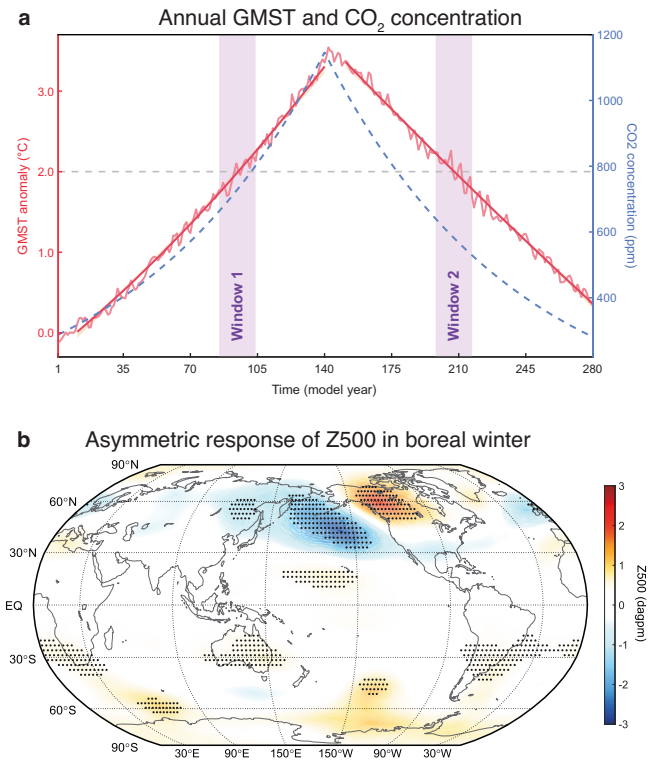

Fig. 1 | Hysteresis of annual GMST and atmospheric circulation in boreal winter. **a** Temporal evolution of the GMST anomaly (unit: °C; pink line) and CO_2 concentration (unit: ppm; blue line). The red lines denote the GMST secular trends obtained by the EEMD analysis, with orange shading indicating the 99% confidence interval. The horizontal gray line indicates the 2 °C global warming level, and two purple shadings represent 20-year-long windows at Year 85–104 (ramp-up) and 198–217 (ramp-down), respectively. **b** Asymmetric response of 500 hPa geopotential height (unit: dagpm) in boreal winter. Stippling indicates where changes are statistically significant at a 95% confidence level based on a two-sided Student's *t*-test.

maps of the two periods. The winter precipitation in Window 1 exhibits positive anomalies from the Pacific Northwest to northern California, while the wetter condition emerges in Window 2 over the Gulf of Alaska and northern California with remarkable westward extension into the Northeastern Pacific (Fig. 2d, e). We note here that a similar result can be obtained if the length of each window is extended to 30 years or longer. To further examine the robustness, a total of eight models from the CMIP6 archive[7,45] were also analyzed (see Methods and Supplementary Fig. S1). It is found that both the pattern and magnitude are similar (Fig. 2f, g and Supplementary Fig. S2), indicating the robustness of the hysteresis of winter NPWNA precipitation.

To understand its formation, we performed an atmospheric water vapor budget analysis[47–49] (see Methods). The net precipitation (precipitation minus evaporation; Fig. 3a) displays similar features with precipitation (Fig. 2b), suggesting that the asymmetric change in winter precipitation is mostly induced by an anomalous moisture flux convergence or divergence instead of changing in-situ evaporation (Supplementary Fig. S3a). The monthly moisture transport can explain most of the tripolar structure (Fig. 3b), although the sub-monthly term (mainly due to transient eddies) cannot be completely negligible (Fig. 3c). We further decompose the monthly moisture transport anomalies into the dynamic (Fig. 3d) and thermodynamic (Fig. 3e) terms, the former of which highly matches the "wetter-drier-wetter" pattern, indicating that the asymmetric change in mean atmospheric circulation is the key factor. The small magnitude of the residual term supports the validity of this decomposition method (Fig. 3f and Supplementary Fig. S3b–d). The result highlights the importance of the cyclonic circulation change over the North Pacific, corresponding to an intensification of the Aleutian low (AL; Figs. 1b, 4b), for the formation of the asymmetric precipitation change.

Linking precipitation change to the SST pattern

Changes in precipitation may be attributed to three factors, including the CO_2 direct effect, global mean sea surface temperature (GMSST) difference, and the SST pattern[49]. In particular, the CO_2 direct effect refers to the fast adjustments of the land and atmosphere due to the radiative forcing difference between Windows 2 and 1. Its contribution is evaluated by using the so-called Hansen experiment[26,50,51] (see Methods and Supplementary Fig. S4). In addition, the GMSST effect is estimated by locating Window 3 (Supplementary Fig. S5), where the GMSST anomaly is the same as Window 1 (see Methods and Supplementary Fig. S6). However, it is found that these two effects are almost negligible, which implies that the asymmetric response of the SST pattern is the major candidate.

The asymmetric response of the global SST pattern is demonstrated in Fig. 4a. An El Niño-like SST warming pattern emerges over the tropical central-eastern Pacific, resulting in a Pacific Decadal Oscillation-like pattern over the North Pacific via atmospheric bridge[52]. Besides, a wide and almost uniform warming pattern can be found over the Southern Ocean. In contrast, the North Atlantic shows a strong cooling. Those features are highly consistent with the previous findings supported by different climate models[18,20,42]. As one of the well-discussed ENSO extratropical teleconnection patterns, a strengthening signal of the AL is observed in boreal winter[53] (Fig. 4b). However, the AL intensification and tripolar precipitation change pattern is not fully attributable to the conventional ENSO teleconnection. Indeed, the response efficiency of the AL's intensity (e_{AL}) during boreal winter, which is measured by the North Pacific Index (NPI)[54,55] scaled with the SST anomaly over the Niño3.4 region, is much larger than that inferred from ENSO in the 800-year piControl simulation of the same model (Fig. 4c). This suggests the existence of another important mechanism.

In addition to the El Niño-like zonal SST gradient, the tropical Pacific SST pattern features a meridional contrast between the Northern and Southern Hemisphere (Figs. 4a, 5a). This feature can also be found in CESM1.2 large ensemble experiment[18,42] and a sensitivity experiment driven by uniform deep ocean warming[42], suggesting robustness. Here, we investigate its potential influence on the AL with atmospheric general circulation model (AGCM) experiments using GFDL AM2.1[56] driven by an idealized

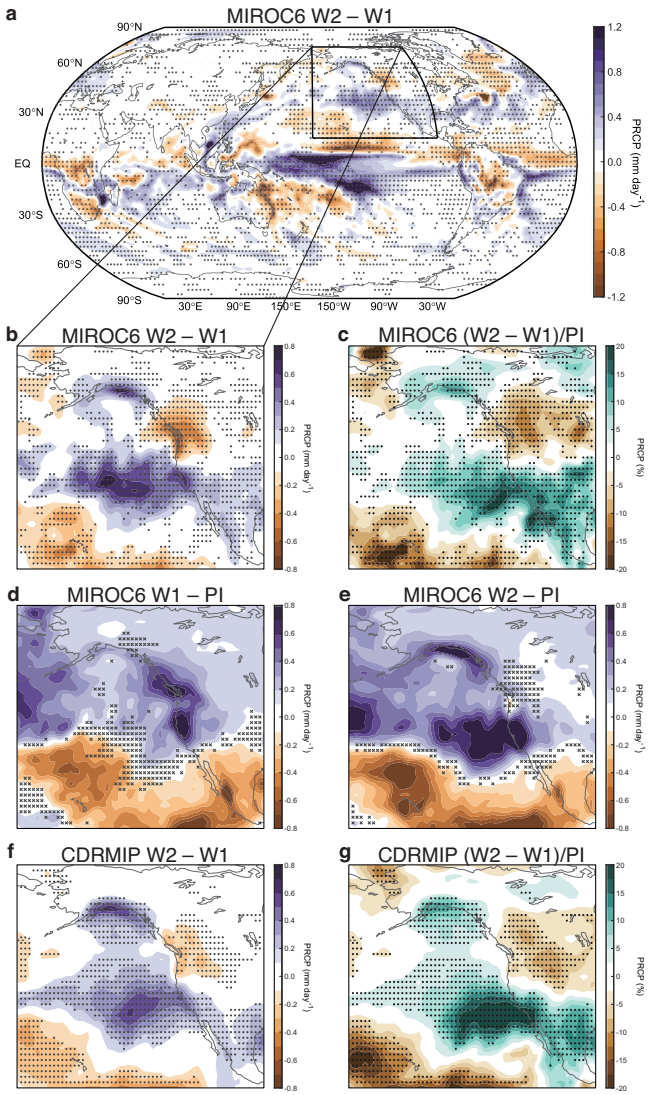

Fig. 2 | Irreversibility of boreal winter precipitation. a Asymmetric response of global precipitation (unit: mm day $^{-1}$) in boreal winter. **b** Same as (**a**), but only highlights the NPWNA region. **c** Same as (**b**), but for percentage change (unit: %) relative to the piControl climatology. **d**, **e** Precipitation anomalies (unit: mm day $^{-1}$) in boreal winter in Windows 1 and 2, respectively. **f**, **g** Same as (**b**, **c**), respectively, but from the CMIP6 CDRMIP dataset. Stippling in (**a**–**c**) indicates that at least four of the five members (80%) agree on the sign of the ensemble mean, while that in **f**, **g** indicates where changes are statistically significant at a 95% confidence level using two-sided Student's *t*-test. Crosses in **d**, **e** indicate that at least one member disagrees with the sign of the ensemble mean.

SST anomaly dipole (warm and cold patches) on the SST climatology (see Methods and Fig. 6a). Figure 6 shows the large-scale atmospheric response during boreal winter. In the middle troposphere, a pattern that projects onto the West Pacific (WP) pattern[57] emerges, which is accompanied by an AL intensification at the surface (Fig. 6a, b). Besides, the "wetter-drier-wetter" tripolar precipitation response pattern over the NPWNA is also reproduced (Fig. 6c, d). Those results provide evidence for the role of the equatorially asymmetric SST change pattern in the tropical Pacific.

The next question is, how does the equatorially asymmetric SST anomalies drive the AL strengthening? Based on hydrological constraints, it is noted that precipitation over the Maritime Continent and Australian summer monsoon region enhances in response to the meridional SST gradient (Fig. 6c). Indeed, in the Window 2 – Window 1 precipitation difference, negative signals over the Maritime Continent region are not clear (Fig. 2a) despite the El Niño-like SST anomaly, presumably due to the influence of the meridional SST gradient. There is evidence that these precipitation enhancements over the Maritime Continent and northern Australia can excite the WP-like pattern through an anomalous local Hadley circulation that extends to the Northern Hemisphere subtropical jet and induces a Rossby wave source[58]. This is corroborated by our linear baroclinic model (LBM)[59] experiment forced by diabatic heating in the north of Australia (see Methods; Supplementary Fig. S7a). As a result, the AL anomaly is further enhanced and causes a surplus or deficit of moisture transport, affecting the NPWNA climate (Fig. 6c, d).

We further examine the potential contribution of precipitation anomalies in the tropical central-eastern Pacific shown in Fig. 6c by using the LBM. The anomalous heating across the equatorial central-eastern Pacific can also contribute to the AL strengthening (Supplementary Fig. S7c), which is similar to the response to El Niño. However, its effect is completely nullified by the concurrent cooling in the north off-equatorial central-eastern Pacific (Supplementary Fig. S7b, d), which is linked with the southward shift of the ITCZ as discussed later. These results further suggest the critical role of the precipitation anomalies over the Maritime Continent and the Australian summer monsoon region in intensifying the AL.

Hysteresis of the tropical Pacific SST gradient with its mechanism

As we discussed above, the hysteresis of the SST pattern over the tropical central-eastern Pacific is the key driver for the AL intensification and the tripolar precipitation pattern in boreal winter. By subtracting the GMSST difference, the SST pattern exhibits both zonal and meridional gradients in the tropical central-eastern Pacific (Fig. 5a).

Regarding the formation of zonal SST gradient, three factors should be discussed. The first is subsurface warming. During the ramp-up period, the deep ocean absorbs a substantial amount of surplus energy, which is kept in the subsurface layer. When the CO_2 concentration starts to decrease, the ocean mixed layer will be chilled from the surface efficiently, while a recalcitrant warming signal will be retained in the subsurface ocean, reducing the ocean's thermal stratification (Supplementary Fig. S8). As a result, the hysteresis of subsurface warming can be brought to the surface continuously by climatological upwelling, which is strong in the eastern equatorial Pacific, leading to the zonally differential SST warming. Second, the subtropical cell brings the water masses submerged in the subtropics to the tropical surface in the thermocline on decadal to multi-decadal timescales[60,61]. During the ramp-down period, the water masses emerging to the equatorial surface originate from periods when the CO_2 concentration is higher, namely a warmer world, yet the opposite way is true in the ramp-up period. After those two processes explained above trigger the initial tendency, the Bjerknes feedback, as the third one, amplifies the weakening of the zonal SST gradient and the Walker circulation (WC; Fig. 5a, b), further exacerbating asymmetric warming.

In addition, but no less vital, the tropical SST pattern also exhibits a meridional gradient (Fig. 5a, c). As shown in Fig. 5a, the meridional SST gradient is combined with cross-equatorial northerlies. This asymmetric change is associated with the meridional precipitation gradient, which displays a nonlinear evolution to CO_2 forcing with a jump in the ramp-down period and a peak at the second 2 °C threshold[18] (Fig. 5c). This feature is likely linked to the hysteresis of the ITCZ position, as also found in the AGCM idealized experiment (Fig. 6c, d). So, what are the physical processes and potential mechanisms that lead to such a meridional SST gradient?

From the global-scale perspective, in the ramp-down period, due to the large heat capacity, the Southern Ocean gradually releases heat to resist radiative cooling. At the same time, the AMOC demonstrates a weakening behavior[18,22,30,42], resulting in North Atlantic cooling via reducing poleward heat transport. Such an interhemispheric energy imbalance must be compensated by the northward cross-equatorial atmospheric energy transport, forcing the ITCZ to shift to the south[18,30,32,62]. The nonlinear jump in the meridional precipitation gradient, as shown by a preceding study[18] suggests the primary role of the global-scale energy transport.

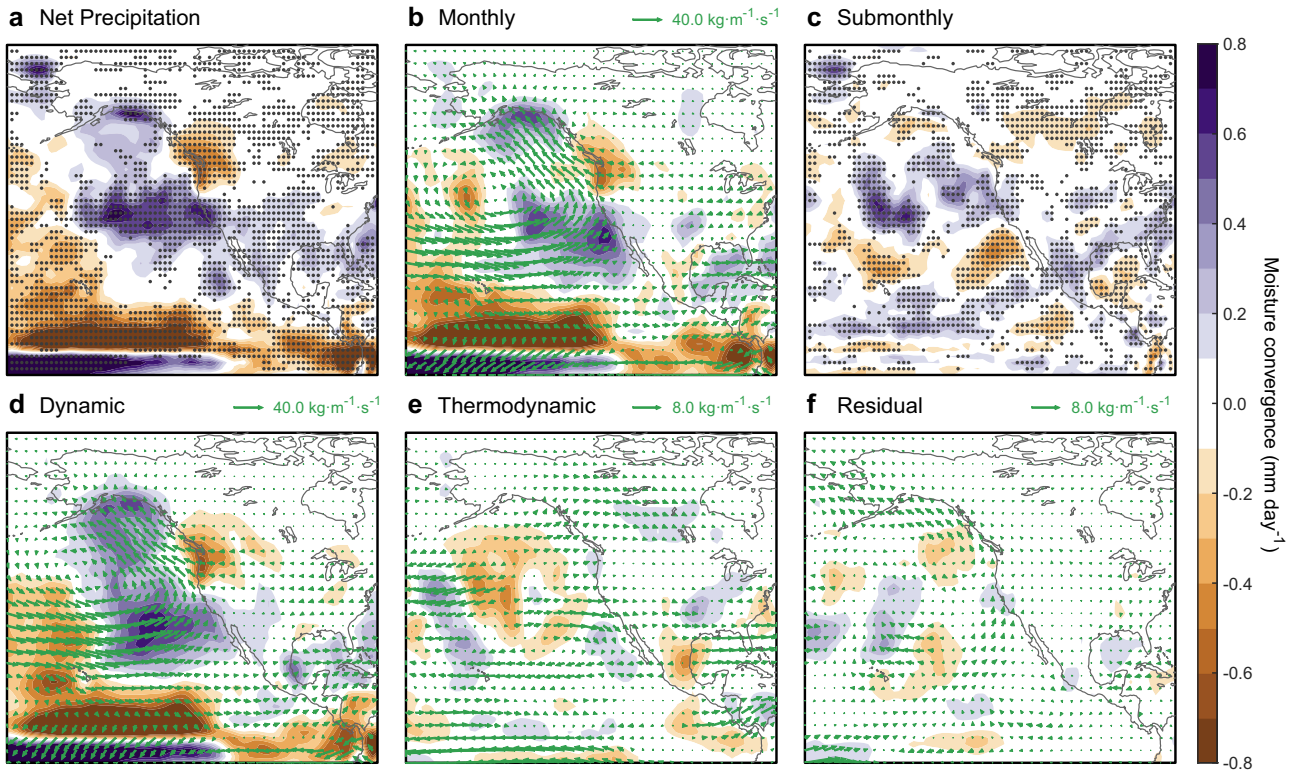

Fig. 3 | Atmospheric moisture budget. Asymmetric change in **a** net precipitation (P – E) in boreal winter, and its decomposition into **b** monthly and **c** sub-monthly terms. The monthly term is further decomposed into **d** dynamic, **e** thermodynamic, and **f** residual terms. Stippling in **a**, **c** indicates that at least four of the five members (80%) agree on the sign with the ensemble mean. Vectors show an asymmetric change in column-integrated moisture flux (**b**) and its decomposition into the contributions from wind change (**d**), humidity change (**e**), and the residual (**f**).

While this delayed energy contrast can determine the response direction of the ITCZ, it can be maintained by the wind-evaporation-SST (WES) feedback[63] locally and other atmospheric forcings[64,65]. To assess them quantitatively, we decomposed the asymmetric response of latent heat flux (Q_E; upward is positive; see Methods and Fig. 7). Overall, the SST over the off-equatorial central-eastern Pacific is higher in Window 2 than 1 (Fig. 4a). By subtracting the Q_E increase that is caused directly by the local SST warming (Supplementary Fig. S9), the effects of atmospheric forcings (Q_{EA}; Fig. 7b) can be obtained. We found that the asymmetric signals averaged over the south and north off-equatorial central-eastern Pacific are opposite in sign (Fig. 7b). We further estimated the effects of the WES feedback (Q_{EW}; Fig. 7c) by measuring surface wind changes (see Methods). It is found that the contribution driven by the WES feedback is prominent compared with the remaining factors (Q_{ER}), which are weak but operate in the same direction as the WES feedback (Fig. 7c, d). These processes maintain the SST meridional gradient and ITCZ southward shift in the asymmetric response, which drives the teleconnection to the NPWNA.

Discussion

The present study revealed the irreversibility of winter precipitation over the NPWNA region against CO_2 forcing. In a symmetric changing CO_2 pathway, although global warming can be reversed to 2 °C again with a lower CO_2 concentration, the hydroclimatic regime over the NPWNA region shows a clear hysteresis behavior. An analysis of the atmospheric water vapor budget indicates that the primary factor is the monthly mean moisture transport, which can be further traced back to the large-scale circulation change, that is, the intensification of the AL. Contribution from the asymmetric response of the storm stack activity is minor, though not negligible.

As we defined climatic hysteresis with the same GMST level, all the factors, including CO_2 direct effect, GMSST difference, and SST pattern, are not even consistent. According to the small magnitude of the former two contributions, the irreversible precipitation is linked to the SST pattern, which exhibits a double-peak warm tongue extending to the Southern Hemisphere over the tropical central-eastern Pacific. The zonal SST gradient is like conventional El Niño events, which is explained by the distinct timescale difference between surface and subsurface warming, and ocean dynamical processes, amplified via the Bjerknes feedback. In addition, we found that the meridional SST gradient may work jointly. Indeed, a set of AGCM experiments confirmed the impact of the meridional SST gradient on the AL intensification. The anomalous signal is conveyed to the mid-latitude North Pacific via the local Hadley circulation over the Maritime continent and northern Australia, which then drives Rossby waves, eventually contributing to the formation of the precipitation pattern. A schematic diagram is shown in Fig. 8.

Unlike most previous studies based on the same CO_2 concentration, our focus here is on the asymmetric change in regional hydrological regimes at a fixed warming level, specifically the 2 °C threshold proposed by the Paris Agreement. The findings act as a cautionary signal to us, particularly amidst the unchecked emission of greenhouse gases. Our scientific community has been striving to find solutions for existing climate change. However, almost all the research on the CO_2 removal method indicates that even if this currently hypothetical approach can regulate the global mean evolution, it would still leave irreversible risks to regional climate closely linked to human livelihoods.

Lastly, it should be pointed out that our MIROC6 simulations employed are forced by prescribed atmospheric CO_2 concentration. Such an experiment setting does not account for some physical processes, such as the nonlinear effect of air-sea CO_2 exchange. With CO_2 concentration gradually

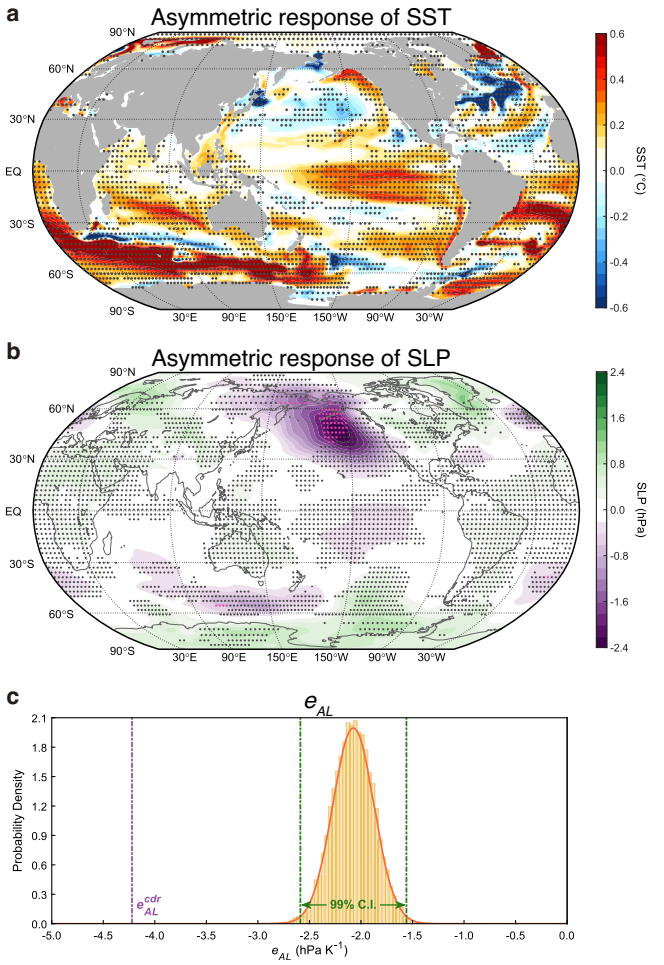

Fig. 4 | Asymmetric response of SST and SLP. a Asymmetric change in SST (unit: °C) in boreal winter. **b** Same as (**a**), but for the SLP (unit: hPa). Black dots indicate that at least four of the five members (80%) agree on the sign of the ensemble mean, and pink dots denote where the values are lacking sign consistency but statistically significant at a 95% confidence level based on a two-sided Student's *t*-test. **c** Probability density function of the e_{AL} in the 800-year-long piControl simulation. Vertical green and purple lines indicate the 99% confidence interval and the e_{AL} from the CDR scenario, respectively.

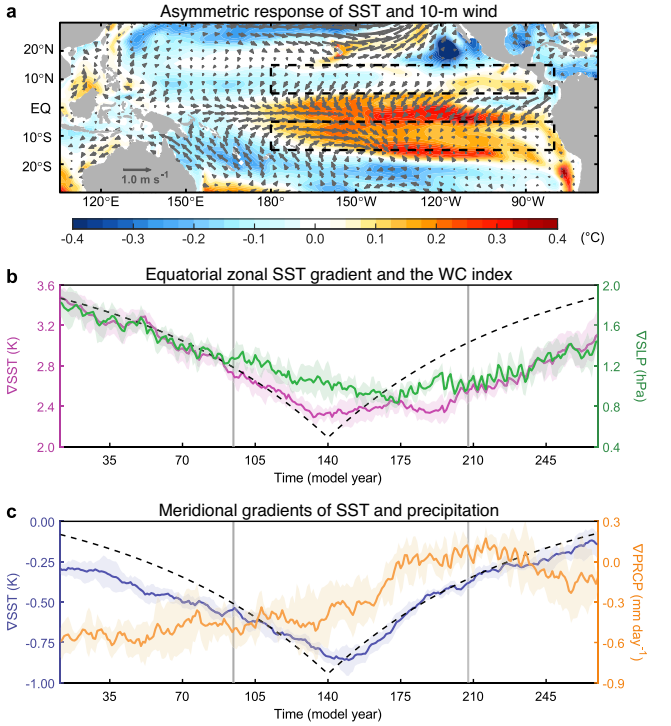

Fig. 5 | Hysteresis of zonal and meridional SST gradient. a Same as Fig. 4a, but highlights the tropical Pacific with GMSST difference subtracted. Vectors show the asymmetric change of 10-meter wind. Black boxes represent the south (15°S-5°S) and north (5°N-15°N) off-equatorial central-eastern Pacific (180°-80°W). **b** Time series of the zonal SST gradient (pink line) and WC index (green line) in boreal winter. **c** Same as (**b**), but for the meridional SST (blue line) and precipitation gradients (orange line). All the curves are smoothed by a 21-year running mean. Shading indicates the 95% confidence interval. Black dashed lines indicate CO_2 concentration (multiplied by -1 for comparison). Vertical gray lines show timepoints with 2 °C global warming level.

increases, deep ocean warming, along with the weakening of AMOC, can impede the transfer of CO_2 from the atmosphere to the ocean. This factor may potentially exacerbate the challenge of reducing atmospheric CO_2 levels. Our study would be expanded to an emission-driven experimental framework that includes the carbon cycle. Nevertheless, our finding will provide the fundamental mechanism of the NPWNA winter precipitation irreversibility.

Methods

MIROC6 configuration

In the current study, the Model for Interdisciplinary Research on Climate version 6 (MIROC6)[43,44] was mainly employed, which is one of the CMIP6 generation models. This model incorporates the atmosphere (CCSR atmospheric general circulation model, CCSR AGCM), ocean-sea ice (CCSR Ocean Component model version 4.9, COCO 4.9), and land components (Minimal Advanced Treatments of Surface Interaction and Runoff version 6, MATSIRO 6.0). In MIROC6, the atmospheric and land components are configured with a horizontal Gaussian grid of ~1.4° with 81 vertical layers. The ocean-sea ice model utilizes a tripolar coordinate system. In the spherical coordinate portion south of 63°N, it has a nominal 1° horizontal resolution (meridional grid spacing around 0.5° near the equator), with 62 vertical ocean levels.

Carbon dioxide removal experiment

We conducted CO_2 ramp-up and ramp-down simulations using MIROC6 with its fully coupled mode, adhering to the protocols of CDRMIP[45], that is, prescribing CO_2 concentration increasing from the preindustrial level (1×CO_2, 284.7 ppm) at a rate of 1% per year until quadrupling (4×CO_2, 1138.8 ppm) over 140 years, then symmetrically decreasing at the same rate for another 140 years until reaching its initial level (1×CO_2). All the other radiative forcing factors were fixed at preindustrial levels. Five members with different initial conditions were randomly extracted from the 800-year-long piControl simulation to cancel internal variability. The reference climatology was derived from the last 100 years of the piControl simulation. The results are considered robust when at least four of the five members agree with the sign of the ensemble mean. In addition, the two-sided Student's *t*-test was also employed for assessing statistical significance, and Satterthwaite's approximation was used to estimate the effective degrees of freedom[66]. Unless otherwise noted, the results of the present study are based on MIROC6.

CMIP6 dataset

In addition to MIROC6, a total of eight models which participated in CDRMIP[45], including ACCESS-ESM1-5, CanESM5, CESM2, CNRM-ESM2-1, GFDL-ESM4, MIROC-ES2L, NorESM1-LM, and UKESM1-0-LL, were also examined. To obtain a similar scenario, the first 140 years of the 1pctCO_2 (ref. 7) and 1pctCO2-cdr (ref. 45) experiments were combined. Each model has only one ensemble member. Like MIROC6, the climatology

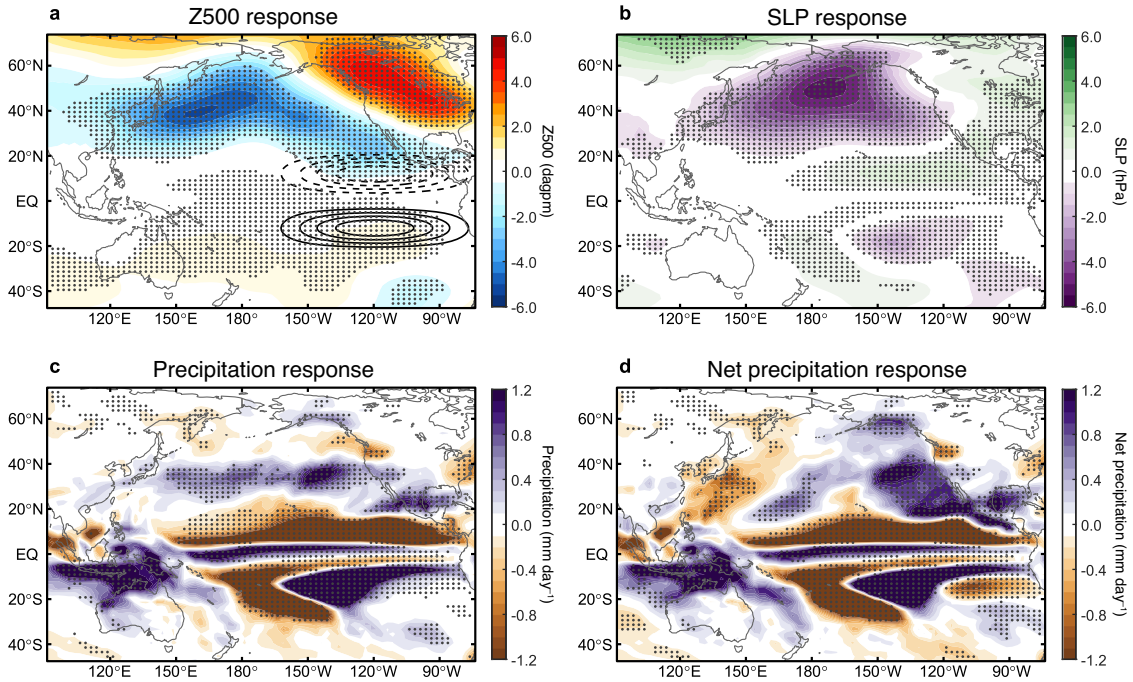

Fig. 6 | Atmospheric response to a meridional SST gradient. Response of (**a**) 500 hPa geopotential height (unit: dagpm), (**b**) SLP (unit: hPa), (**c**) precipitation (unit: mm day $^{-1}$), and (**d**) net precipitation (P – E, unit: mm day $^{-1}$) to an idealized meridional SST gradient forcing during boreal winter in AM2.1. Solid (dashed) contours in (**a**) show the imposed SST warm (cold) patch, with intervals of 0.4 °C (zero line is omitted for clarity). Stippling indicates where changes are statistically significant at a 99% confidence level using a two-sided Student's *t*-test.

was also defined as the last 100 years from the piControl simulation, except UKESM1-0-LL, where the first 100 years were used because of data missing. The CMIP6 dataset was analyzed after being bilinearly interpolated onto the identical horizontal grid as MIROC6. More details of these eight models are available in Supplementary Table 1.

Definition of the 2 °C warming points

To estimate global warming objectively, a method named ensemble empirical mode decomposition (EEMD)[67,68] was applied. This method has been widely used for nonlinear and nonstationary climatic analyses, particularly powerful for extracting low-frequency signals[69,70]. In EEMD, a given time series ($Y(t)$) can be decomposed into a finite number of intrinsic mode functions (IMFs) and a residual term ($R(t)$):

$$Y(t) = \sum_{i=1}^{N} \mathrm{IMF}_i(t) + R(t) \tag{1}$$

where N, the number of IMFs, is determined as the binary logarithm of the time series length (round down)[68]. Note that the residual term, also termed secular trend, can be viewed as the transient response to external forcing.

In this study, GMST was defined as the annual average of near-surface air temperature, and the EEMD was applied to the GMST anomaly time series. The EEMD parameters, including the variance of white noise relative to the input data and the ensemble members, were set to 0.2 and 400 times, respectively. To avoid any interference caused by the artificial turning point of radiative forcing, the EEMD decomposition was executed separately for two parts: Years 11–140 in ramp-up and 151–280 in ramp-down. Based on the secular trends, two 2 °C warming points were identified, centered on which Windows 1 and 2 were defined. In MIROC6, each window spanned 20 years, while it extended to 40 years in CMIP6 due to the varied amplitudes of internal variability across models. We declare that the results are not sensitive to the parameter settings and time interval selection. The confidence interval was estimated using the bootstrap method (see below section).

Bootstrap method

In this study, a bootstrap method[71] was utilized to estimate the confidence interval. Generally, regarding a given variable in MIROC6, its values from five members were randomly resampled to generate 10,000 realizations. Note that a specific member can be selected multiple times. Then, they were sorted in descending order. For example, the range between the 250th and 9750th values indicates a 95% confidence interval.

For the secular trend extracted by EEMD, its confidence interval was estimated by following steps: (1) Subtract the secular trend from the raw data to obtain a residual sequence; (2) Permute the elements within the residual sequence randomly to yield 10,000 instances; (3) For each instance, add back the original secular trend; (4) Execute EEMD decomposition for each case to extract secular trend. The 99% confidence interval is then determined by the 0.5th and 99.5th percentiles.

Atmospheric water vapor budget

The atmospheric water vapor budget can be written as[48,49]:

$$-\nabla_p \cdot \int_{p_{top}}^{p_{surf}} (\boldsymbol{u}q)\frac{dp}{g} = P - E + \frac{\partial Q}{\partial t} \tag{2}$$

where ∇_p is the horizontal divergence in the pressure coordinate, $\boldsymbol{u}$ is the horizontal wind velocity, p is the pressure, q is the specific humidity, g is the gravitational acceleration, P is the precipitation, E is the evaporation, and $Q = \int_{p_{top}}^{p_{surf}} q\frac{dp}{g}$ indicates the atmospheric total precipitable water, with its time tendency $\left(\frac{\partial Q}{\partial t}\right)$ being negligible on monthly or longer timescales[18,49]. Therefore, the net precipitation ($P - E$, right side) should be balanced by the horizontal moisture flux convergence integrated vertically from the surface to the top of the atmosphere (left side).

For a given variable (e.g., P) in boreal winter, here we denote its monthly mean as $\bar{P}$, anomaly as P', sub-monthly deviation as P^*, asymmetric change (Window 2 minus 1) as ΔP, and climatology in Window 1 or 2 by subscript. Then, the asymmetric change of net precipitation can be decomposed into monthly and sub-monthly terms, the latter of which is

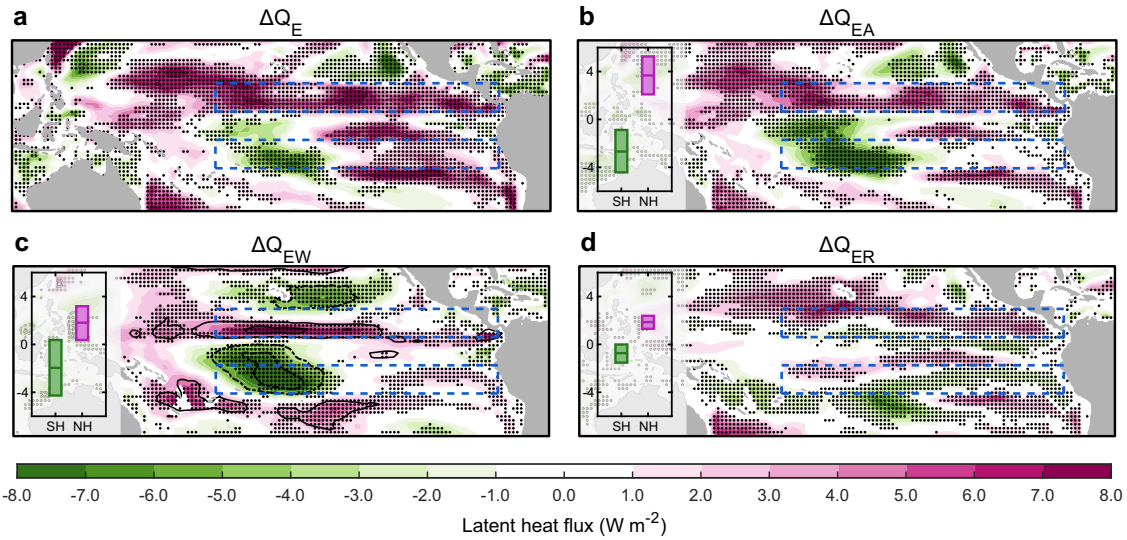

Fig. 7 | Latent heat flux decomposition. Asymmetric change in (**a**) ΔQ_E, (**b**) ΔQ_{EA}, (**c**) ΔQ_{EW}, and (**d**) ΔQ_{ER}. Stippling indicates that at least four of the five members (80%) agree on the sign of the ensemble mean. Bar plots in **b**–**d** show area-averaged changes (in W m^{-2}) over the south and north off-equatorial central-eastern Pacific (blue boxes, same as Fig. 5a). The bar represents the 5th–95th percentile range. Solid (dashed) contours in **c** show the positive (negative) asymmetric changes in scalar wind speed at the sea surface with intervals of 0.15 m s^{-1} (zero line is omitted for clarity).

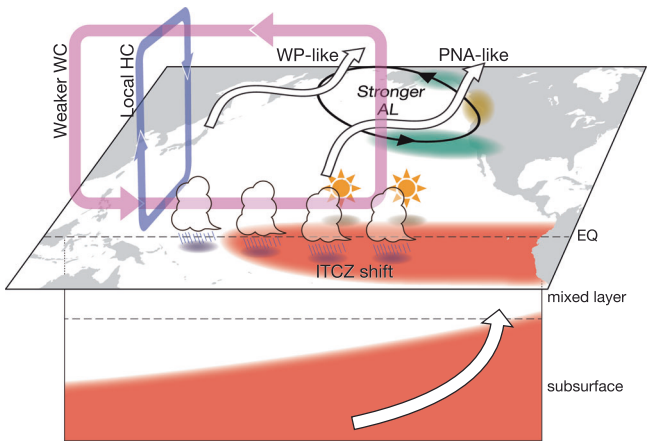

Fig. 8 | A schematic diagram of the key mechanisms related to the asymmetric response of winter precipitation over the NPWNA under the CDR scenario. Two critical processes are involved. The first one is PNA-like teleconnection. In the tropical central-eastern Pacific, the delayed subsurface warming results in surface SST warming, which is amplified via Bjerknes feedback. This zonal SST gradient influences winter precipitation over the NPWNA by triggering a PNA-like wave-train. The second one is WP-like teleconnection. In the ramp-down period, the ITCZ position shifts southward due to interhemispheric energy redistribution, which is mainly maintained by the WES feedback. As a result, the meridional SST gradient emerges. By enhancing precipitation over the Maritime Continent and Australian summer monsoon region, the meridional SST gradient excites the WP-like teleconnection pattern through an anomalous local Hadley circulation that extends to the Northern Hemisphere subtropical jet and induces a Rossby wave source, eventually contributing to the asymmetry of hydrological cycle over the NPWNA.

mostly manifested as the transient eddy activity[48,49]:

$$\underbrace{\Delta\left(\bar{P}-\bar{E}\right)}_{\text{Net precipitation}} = \underbrace{\Delta\left[-\int_{p_{top}}^{p_{surf}}\nabla_p\cdot\left(\bar{\boldsymbol{u}}\bar{q}\right)\frac{dp}{g}\right]}_{\text{Monthly Term}} + \underbrace{\Delta\left[-\int_{p_{top}}^{p_{surf}}\nabla_p\cdot\left(\boldsymbol{u}^{*}\bar{q}^{*}\right)\frac{dp}{g}\right]}_{\text{Sub}-\text{monthly term}} \quad (3)$$

Note that the sub-monthly term was calculated as a residual of the above equation due to the unavailability of instantaneous model outputs. The monthly term can be further decomposed into dynamic, thermodynamic, month-to-month covariance, and second-order terms:

$$\underbrace{\Delta\left[-\int_{p_{top}}^{p_{surf}}\nabla_p\cdot\left(\bar{\boldsymbol{u}}\bar{q}\right)\frac{dp}{g}\right]}_{\text{Monthly Term}} = \underbrace{\left(-\int_{p_{top}}^{p_{surf}}\nabla_p\cdot\left(\bar{q}_1\Delta\bar{\boldsymbol{u}}\right)\frac{dp}{g}\right)}_{\text{Dynamic Term}} + \underbrace{\left(-\int_{p_{top}}^{p_{surf}}\nabla_p\cdot\left(\bar{\boldsymbol{u}}_1\Delta\bar{q}\right)\frac{dp}{g}\right)}_{\text{Thermodynamic Term}} + \underbrace{\left(-\int_{p_{top}}^{p_{surf}}\nabla_p\cdot\left[\left(\bar{\boldsymbol{u}}'\bar{q}'\right)_2-\left(\bar{\boldsymbol{u}}'\bar{q}'\right)_1\right]\frac{dp}{g}\right)}_{\text{Month}-\text{to}-\text{month covariance term}} + \underbrace{\left(-\int_{p_{top}}^{p_{surf}}\nabla_p\cdot\left[\left(\Delta\bar{\boldsymbol{u}}\Delta\bar{q}\right)\right]\frac{dp}{g}\right)}_{\text{Second}-\text{order Term}} \quad (4)$$

where the sum of the last two terms was referred to as the residual term (Fig. 3f).

Precipitation pattern decomposition

A precipitation change pattern can be caused by three factors, including CO_2 direct effect, GMSST difference, and SST pattern[49]:

$$\Delta P = \Delta P_{CO2} + \Delta P_{GMSST} + \Delta P_{SST}. \quad (5)$$

To investigate the CO_2 direct effect, we used the Hansen experiment[26,50,51] with MIROC6 AGCM. In the control run (PI-SST), both SST and sea ice were fixed as piControl climatology, and all radiative forcing factors were set at a preindustrial level. In the sensitivity run (PI-SST-4xCO2), the same setting was used, but the CO_2 concentration is quadrupled. Both PI-SST and PI-SST-4xCO_2 runs were integrated for up to 50 years, with only the last 40 years being considered for our analysis. The CO_2 direct effect can be estimated by linearly scaling the radiative forcing gap

between Windows 2 and 1 (ref. 51):

$$\Delta P_{CO_2} = \left(\frac{\ln CO_2{}^{win2} - \ln CO_2{}^{win1}}{\ln 4}\right)\Delta P_{rapid} \quad (6)$$

where ΔP_{rapid} represents the precipitation change due to rapid adjustment, calculated as boreal winter climatology anomaly (PI-SST-4xCO_2 minus PI-SST).

We estimated the GMSST effect as follows: Firstly, with the same procedure as for GMST, executing EEMD decomposition on annual GMSST anomaly. Subsequently, another 20-year-long window, Window 3, with the same GMSST anomaly as Window 1 was identified (Supplementary Fig. 3a). The GMSST effect was then calculated by the boreal winter climatology difference (Window 2 minus 3).

Response efficiency of the AL to Niño3.4 SST

In the boreal winter, the enhancement of the AL is widely recognized as one of the most pronounced extratropical ENSO teleconnections in the Northern Hemisphere[52,53], modulating the precipitation pattern over the NPWNA. Here, the North Pacific Index (NPI)[55] was used to represent the AL intensity (I_{AL}), which is defined as the area-averaged SLP anomalies over the North Pacific (30°N-65°N, 160°E-140°W). Then, its response efficiency to Niño3.4 SST in boreal winter can be written as:

$$e_{AL} = \frac{I_{AL}}{SSTA_{Niño3.4}} \quad (6)$$

where $SSTA_{Niño3.4}$ denotes the area-averaged SST anomaly over the Niño 3.4 region (5°S-5°N, 170°W-120°W)[54]. In Fig. 4c, we selected 105 winters from the piControl simulation where $SSTA_{Niño3.4}$ exceeds one standard deviation. The e_{AL} was calculated for these selected winters. After resampling 10,000 times, we fitted them to a normal distribution to derive the 99% confidence interval.

Definition of climate indices

1. The zonal SST gradient is defined as the SST difference between the western Pacific (5°S-5°N, 80°E-160°W) and Niño 3 region (5°S-5°N, 150°W-90°W)[26,33].

2. The WC index is defined as the SLP difference between the equatorial eastern Pacific (5°S-5°N, 160°W-80°W) and Indo-western Pacific (5°S-5°N, 80°E-160°E)[72].

3. The meridional SST gradient is defined as the difference in area-weighted SST between the south (15°S-5°S, 180°-80°W) and north (5°N-15°N, 180°-80°W) off-equatorial central-eastern Pacific (Black boxes in Fig. 5a).

4. The meridional precipitation gradient is defined similarly to the meridional SST gradient but using precipitation as the variable and excluding land.

Latent heat flux decomposition

The latent heat flux (Q_E, upward is defined as positive) at the open ocean surface may be cast as[63]:

$$Q_E = \rho_a L C_E W\left[q_s(T) - RHq_s(T - T_d)\right] \quad (7)$$

where ρ_a is the surface air density, L is the latent heat of evaporation, C_E is the nondimensional bulk transfer coefficient, W is the scalar wind speed at the sea surface, RH is the relative humidity of the surface air, T is the SST, T_d is the sea minus air temperature difference, and $q_s(T)$ is the saturated specific humidity, following the Clausius-Clapeyron relation. Therefore, the asymmetric change of Q_E in the CDR scenario arises from contributions from both atmospheric conditions (including W, RH, and T_d) and SST:

$$\Delta Q_E = \Delta Q_{EA} + \Delta Q_{EO} \quad (8)$$

where Δ denotes the difference in boreal winter climatology between Windows 2 and 1, and subscripts A and O represent atmospheric forcing and oceanic response, respectively. For ΔQ_{EO}, by linearizing Eq. (7) as a Newtonian cooling term, we have[64,65]:

$$\Delta Q_{EO} = \bar{Q}_E\left(\frac{1}{q_s}\frac{dq_s}{dT}\right)\Delta T \quad (9)$$

where the overbar denotes climatology in boreal winter. The ΔQ_{EA} is then calculated as the residual. The portion attributed to the WES feedback is estimated as[64]:

$$\Delta Q_{EW} = \bar{Q}_E\frac{\Delta W}{\bar{W}} \quad (10)$$

and the residual term infers the contribution from the other atmospheric factors:

$$\Delta Q_{ER} = \Delta Q_{EA} - \Delta Q_{EW} \quad (11)$$

Meridional SST dipole AGCM experiment

To examine how the atmosphere will respond to the meridional SST gradient, we conducted experiments using Geophysical Fluid Dynamics Laboratory atmospheric model version 2.1 (GFDL AM2.1)[56], which is configured with a horizontal resolution of 2° × 2.5° latitude-longitude with 24 vertical levels. In the control run, the atmosphere was forced with repeating SST and sea ice climatological seasonal cycles, from the U.S. National Oceanic and Atmospheric Administration (NOAA) Optimum Interpolation SST V2 dataset[73]. For the sensitivity run, an idealized meridional SST dipole was imposed to the climatology, characterized by a warming patch in the south and a cold patch in the north off-equatorial central-eastern Pacific. To avoid nonlinearity effects induced by unrealistic SST gradients, each anomaly patch followed a localized cosine hump function[74,75]:

$$SSTA(lon, lat) = A\cos^2\left(\frac{\pi}{2}\frac{lon - lon_c}{lon_w}\right)\cos^2\left(\frac{\pi}{2}\frac{lat - lat_c}{lat_w}\right) \quad (12)$$

on the rectangle $lon_c \pm lon_w$, $lat_c \pm lat_w$, and zero elsewhere. In Eq. (12), A is the amplitude of the imposed SST anomaly, and the subscripts c and w denote the center and half-width of the patch, respectively. In this study, the values of A and lat_c were set to 2K and 12°S for the warm patch, while those of the opposite signs were used for the cold patch. The other settings were set at $\phi_w = 24°$, $\lambda_c = 120°$W, and $\lambda_w = 120°$. Both the control and sensitivity runs were integrated for 51 years, with the first year being discarded as a spin-up.

LBM experiments

To investigate the atmospheric response to diabatic forcing, the dry version of the LBM[59] was employed. This model is based on the primitive equations linearized about the DJF climatology of the JRA-55 reanalysis dataset[76] for 1959–2019, and has a horizontal resolution of T42 (~2.8°) with 20 vertical σ layers. Linear damping was imposed with an e-folding time of 1 day at $\sigma \geq 0.945$ and $\sigma \leq 0.025$, 5 days at $\sigma = 0.9$, 15 days at $\sigma = 0.83$, and 30 days at $0.035 \leq \sigma \leq 0.745$. The model was forced by prescribed diabatic heating (cooling) with a peak of +1 (–1) K day^{-1} at $\sigma = 0.45$. The simulation was integrated for 60 days, and the average over the last 30 days are shown.

Data availability

Optimum Interpolation SST data can be downloaded from the NOAA PSL, Boulder, Colorado, USA, at https://www.esrl.noaa.gov/psd/data/gridded/data.noaa.oisst.v2.html. All the CMIP6 outputs used in this research are freely available online at https://esgf-node.llnl.gov/projects/cmip6/. Data for

MIROC6, GFDL AM2.1, and LBM simulations used in the current study are available upon reasonable request from the authors.

Code availability

MATLAB R2022b is mainly used for analyzing the data and producing the figures. All codes used in this study are available upon reasonable request from the first author, Zhenhao Xu (zhenhao_xu@atmos.rcast.u-tokyo.ac.jp).

Received: 13 August 2024; Accepted: 29 November 2024;
Published online: 19 December 2024

References

1. Allen, M. R. et al. Warming caused by cumulative carbon emissions towards the trillionth tonne. *Nature* **458**, 1163–1166 (2009).
2. O'Neill, B. C. et al. IPCC reasons for concern regarding climate change risks. *Nat. Clim. Change* **7**, 28–37 (2017).
3. IPCC. *Climate Change 2021: The Physical Science Basis* (Cambridge Univ. Press, 2021).
4. Taylor, G. & Vink, S. Managing the risks of missing international climate targets. Climate risk management. *Clim. Risk Manag.* **34**, 100379 (2021).
5. Voosen, P. 2023 was the hottest year on record — and even hotter than expected. *Science* **383**, 134 (2024).
6. Witze, A. Earth boiled in 2023 — will it happen again in 2024? *Nature* **625**, 637–639 (2024).
7. Eyring, V. et al. Overview of the coupled model intercomparison project phase 6 (CMIP6) experimental design and organization. *Geosci. Model Dev.* **9**, 1937–1958 (2016).
8. O'Neill, B. C. et al. The scenario model intercomparison project (ScenarioMIP) for CMIP6. *Geosci. Model Dev.* **9**, 3461–3482 (2016).
9. UNFCCC. Adoption of the Paris Agreement FCCC/CP/2015/L.9/Rev.1 (2015).
10. Fuss, S. et al. Betting on negative emissions. *Nat. Clim. Change* **4**, 850–853 (2014).
11. Meinshausen, M. et al. The shared socio-economic pathway (SSP) greenhouse gas concentrations and their extensions to 2500. *Geosci. Model Dev.* **13**, 3571–3605 (2020).
12. Tebaldi, C. et al. Climate model projections from the Scenario Model Intercomparison Project (ScenarioMIP) of CMIP6. *Earth Syst. Dynam.* **12**, 253–293 (2021).
13. Zickfeld, K., Azevedo, D., Mathesius, S. & Matthews, H. D. Asymmetry in the climate-carbon cycle response to positive and negative CO_2 emissions. *Nat. Clim. Change* **11**, 613–617 (2021).
14. Cao, L. & Caldeira, K. Atmospheric carbon dioxide removal: Long-term consequences and commitment. *Environ. Res. Lett.* **5**, 024011 (2010).
15. National Research Council. *Climate Intervention: Carbon Dioxide Removal and Reliable Sequestration* (The National Academies Press, 2015).
16. Caldeira, K., Bala, G. & Cao, L. The science of geoengineering. *Annu. Rev. Earth Planet. Sci.* **41**, 231–256 (2013).
17. Vaughan, N. E. & Lenton, T. M. A review of climate geoengineering proposals. *Clim. Change* **109**, 745–790 (2009).
18. Kug, J.-S. et al. Hysteresis of the intertropical convergence zone to CO_2 forcing. *Nat. Clim. Change* **12**, 47–53 (2022).
19. Boucher, O. et al. Reversibility in an Earth system model in response to CO_2 concentration changes. *Environ. Res. Lett.* **7**, 024013 (2012).
20. Wu, P., Ridley, J., Pardaens, A., Levine, R. & Lowe, J. The reversibility of CO_2 induced climate change. *Clim. Dyn.* **45**, 745–754 (2015).
21. Zickfeld, K., MacDougall, A. H. & Damon Matthews, H. On the proportionality between global temperature change and cumulative CO_2 emissions during periods of net negative CO_2 emissions. *Environ. Res. Lett.* **11**, 055006 (2016).
22. An, S.-I. et al. Global cooling hiatus driven by an AMOC overshoot in a carbon dioxide removal scenario. *Earths Future* **9**, e2021EF002165 (2021).
23. Kim, S.-K. et al. Widespread irreversible changes in surface temperature and precipitation in response to CO_2 forcing. *Nat. Clim. Change* **12**, 834–840 (2022).
24. Wu, P., Wood, R., Ridley, J. & Lowe, J. Temporary acceleration of the hydrological cycle in response to a CO_2 rampdown. *Geophys. Res. Lett.* **37**, L12705 (2010).
25. Cao, L., Bala, G. & Caldeira, K. Why is there a short-term increase in global precipitation in response to diminished CO_2 forcing? *Geophys. Res. Lett.* **38**, 1–6 (2011).
26. Chadwick, R., Wu, P., Good, P. & Andrews, T. Asymmetries in tropical rainfall and circulation patterns in idealised CO_2 removal experiments. *Clim. Dyn.* **40**, 295–316 (2013).
27. Yeh, S.-W., Song, S.-Y., Allan, R. P., An, S.-I. & Shin, J. Contrasting response of hydrological cycle over land and ocean to a changing CO_2 pathway. *npj Clim. Atmos. Sci.* **4**, 1–8 (2021).
28. Zhou, S., Huang, P., Xie, S.-P., Huang, G. & Wang, L. Varying contributions of fast and slow responses cause asymmetric tropical rainfall change between CO_2 ramp-up and ramp-down. *Sci. Bull.* **67**, 1702–1711 (2022).
29. Song, S.-Y. et al. Climate sensitivity controls global precipitation hysteresis in a changing CO_2 pathway. *npj Clim. Atmos. Sci.* **6**, 156 (2023).
30. An, S.-I. et al. General circulation and global heat transport in a quadrupling CO_2 pulse experiment. *Sci. Rep.* **12**, 11569 (2022).
31. Kim, S.-Y. et al. Hemispherically asymmetric Hadley cell response to CO_2 removal. *Sci. Adv.* **9**, eadg1801 (2023).
32. Liu, C. et al. ENSO skewness hysteresis and associated changes in strong El Niño under a CO_2 removal scenario. *npj Clim. Atmos. Sci.* **6**, 117 (2023).
33. Song, S.-Y. et al. Asymmetrical response of summer rainfall in East Asia to CO_2 forcing. *Sci. Bull.* **67**, 213–222 (2022).
34. Oh, H. et al. Contrasting hysteresis behaviors of Northern hemisphere land monsoon precipitation to CO_2 pathways. *Earth's Future* **10**, e2021EF002623 (2022).
35. Paik, S., An, S.-I., Min, S.-K., King, A. D. & Shin, J. Hysteretic behavior of global to regional monsoon area under CO_2 ramp-up and ramp-down. *Earths Future* **11**, e2022EF003434 (2023).
36. Zhang, S., Qu, X., Huang, G. & Hu, P. Asymmetric response of South Asian summer monsoon rainfall in a carbon dioxide removal scenario. *npj Clim. Atmos. Sci.* **6**, 10 (2023).
37. Wu, P., Jackson, L., Pardaens, A. & Schaller, N. Extended warming of the northern high latitudes due to an overshoot of the Atlantic meridional overturning circulation. *Geophys. Res. Lett.* **38**, L24704 (2011).
38. Sgubin, G., Swingedouw, D., Drijfhout, S., Hagemann, S. & Robertson, E. Multimodel analysis on the response of the AMOC under an increase of radiative forcing and its symmetrical reversal. *Clim. Dyn.* **45**, 1429–1450 (2015).
39. Liu, C. et al. Hysteresis of the El Niño–Southern Oscillation to CO_2 forcing. *Sci. Adv.* **9**, eadh8442 (2023).
40. Pathirana, G. et al. Increase in convective extreme El Niño events in a CO_2 removal scenario. *Sci. Adv.* **9**, eadh2412 (2023).
41. Hwang, J. et al. Asymmetric hysteresis response of mid-latitude storm tracks to CO2 removal. *Nat. Clim. Change* **14**, 496–503 (2024).
42. Oh, J.-H. et al. Emergent climate change patterns originating from deep ocean warming in climate mitigation scenarios. *Nat. Clim. Change* **14**, 260–266 (2024).
43. Tatebe, H. et al. Description and basic evaluation of simulated mean state, internal variability, and climate sensitivity in MIROC6. *Geosci. Model Dev.* **12**, 2727–2765 (2019).

44. Kataoka, T. et al. Seasonal to decadal predictions with MIROC6: description and basic evaluation. *J. Adv. Model. Earth Syst.* **12**, e2019MS002035 (2020).
45. Keller, D. P. et al. The carbon dioxide removal model intercomparison project (CDRMIP): rationale and experimental protocol for CMIP6. *Geosci. Model Dev.* **11**, 1133–1160 (2018).
46. Horel, J. D. & Wallace, J. M. Planetary-scale atmospheric phenomena associated with the southern oscillation. *Mon. Weather Rev.* **109**, 813–829 (1981).
47. Trenberth, K. & Guillemot, C. J. Evaluation of the global atmospheric moisture budget as seen from analyses. *J. Clim.* **8**, 2255–2272 (1995).
48. Seager, R., Naik, N. & Vecchi, G. A. Thermodynamic and dynamic mechanisms for large-scale changes in the hydrological cycle in response to global warming. *J. Clim.* **23**(17), 4651–4668 (2010).
49. He, J. & Soden, B. A re-examination of the projected subtropical precipitation decline. *Nat. Clim. Change* **7**, 53–57 (2017).
50. Hansen, J. et al. Efficacy of climate forcings. *J. Geophys. Res.* **110**, D18104 (2005).
51. Zappa, G., Ceppi, P. & Shepherd, T. G. Time-evolving sea-surface warming patterns modulate the climate change response of subtropical precipitation over land. *Proc. Natl Acad. Sci. USA* **117**, 4539–4545 (2020).
52. Trenberth, K. E. et al. Progress during TOGA in understanding and modeling global teleconnections associated with tropical sea surface temperatures. *J. Geophys. Res.* **103**, 14291–14324 (1998).
53. Alexander, M. A. et al. The atmospheric bridge: the influence of ENSO teleconnections on air–sea interaction over the global oceans. *J. Clim.* **15**, 2205–2231 (2002).
54. Barnston, A. G., Chelliah, M. & Goldenberg, S. B. Documentation of a highly ENSO-related SST region in the equatorial Pacific. *Atmos. Ocean* **35**, 367–383 (1997).
55. Trenberth, K. E. & Hurrell, J. W. Decadal atmosphere-ocean variations in the Pacific. *Clim. Dyn.* **9**, 303–319 (1994).
56. Delworth, T. L. et al. GFDL's CM2 global coupled climate models. Part I: formulation and simulation characteristics. *J. Clim.* **19**, 643–674 (2006).
57. Wallace, J. M. & Gutzler, D. S. Teleconnections in the geopotential height field during the Northern Hemisphere winter. *Mon. Weather Rev.* **109**, 784–812 (1981).
58. Sekizawa, S., Nakamura, H. & Kosaka, Y. Remote influence of the interannual variability of the Australian summer monsoon on wintertime climate in East Asia and the Western North Pacific. *J. Clim.* **34**, 9551–9570 (2021).
59. Watanabe, M. & Kimoto, M. Atmosphere–ocean thermal coupling in the North Atlantic: a positive feedback. *Q. J. R. Meteorol. Soc.* **126**, 3343–3369 (2000).
60. McCreary, J. P. & Lu, P. Interaction between the subtropical and equatorial ocean circulations: the subtropical cell. *J. Phys. Oceanogr.* **24**, 466–497 (1994).
61. Gu, D. & Philander, S. G. H. Interdecadal climate fluctuations that depend on exchanges between the tropics and extratropics. *Science* **275**, 805–807 (1997).
62. Liu, W., Li, S., Li, C., Rugenstein, M. & Thomas, A. P. Contrasting fast and slow intertropical convergence zone migrations linked to delayed Southern Ocean warming. *Nat. Clim. Chang.* **14**, 732–739 (2024).
63. Xie, S.-P. & Philander, S. G. H. A coupled ocean-atmosphere model of relevance to the ITCZ in the eastern Pacific. *Tellus* **46A**, 340–350 (1994).
64. Du, Y. & Xie, S.-P. Role of atmospheric adjustments in the tropical Indian Ocean warming during the 20th century in climate models. *Geophys. Res. Lett.* **35**, L08712 (2008).
65. Du, Y., Xie, S.-P., Huang, G. & Hu, K. Role of air-sea interaction in the long persistence of El Niño–induced North Indian Ocean warming. *J. Clim.* **22**, 2023–2038 (2009).
66. Satterthwaite, F. E. An approximate distribution of estimates of variance components. *Biol. Bull.* **2**, 110–114 (1946).
67. Huang, N. E. & Wu, Z. A review on Hilbert-Huang transform: method and its applications to geophysical studies. *Rev. Geophys.* **46**, RG2006 (2008).
68. Wu, Z. & Huang, N. E. Ensemble empirical mode decomposition: a noise-assisted data analysis method. *Adv. Adapt. Data Anal.* **1**, 1–41 (2009).
69. Wu, Z., Huang, N. E., Long, S. R. & Peng, C. K. On the trend, detrending, and variability of nonlinear and nonstationary time series. *Proc. Natl Acad. Sci. USA* **104**, 14889–14894 (2007).
70. Xu, Z. et al. Long-term evolution of global sea surface temperature trend. *Int. J. Climatol.* **41**, 4494–4508 (2021).
71. Austin, P. C. & Tu, J. V. Bootstrap methods for developing predictive models. *Am. Stat.* **58**, 131–137 (2004).
72. Vecchi, G. et al. Weakening of tropical Pacific atmospheric circulation due to anthropogenic forcing. *Nature* **441**, 73–76 (2006).
73. Reynolds, R. W., Rayner, N., Smith, T. M., Stokes, D. & Wang, W. An improved in situ and satellite SST analysis for climate. *J. Clim.* **15**, 1609–1625 (2002).
74. Barsugli, J. J. & Sardeshmukh, P. D. Global atmospheric sensitivity to tropical SST anomalies throughout the Indo-Pacific basin. *J. Clim.* **15**, 3427–3442 (2002).
75. Zhou, C., Zelinka, M. D. & Klein, S. A. Analyzing the dependence of global cloud feedback on the spatial pattern of sea surface temperature change with a Green's function approach. *J. Adv. Model. Earth Syst.* **9**, 2174–2189 (2017).
76. Kobayashi, S. et al. The JRA-55 reanalysis: general specifications and basic characteristics. *J. Meteorol. Soc. Jpn.* **93**, 5–48 (2015).

Acknowledgements

We would like to thank Prof. Axel Timmermann for the useful discussion and Dr. Shion Sekizawa for providing the basic state file for the LBM experiments. This study was jointly funded by the National Natural Science Foundation of China (NSFC; 42141019 and 42261144687), the Japanese Ministry of Education, Culture, Sports, Science and Technology (MEXT) through the Advanced Studies of Climate Change Projection (SENTAN; JPMXD0722680395), the Arctic Challenge for Sustainability II (ArCSII; JPMXD1420318865), and the Japan Society for the Promotion of Science (JSPS) through Grants-in Aid for Scientific Research (JP19H05703, JP23K22570, JP23K25937, JP24H00261, and JP24H02223) and A3 Foresight Program (JPJSA3F20220001). The first author, Zhenhao Xu, was supported by China Scholarship Council (CSC), during his exchange study at the University of Tokyo.

Author contributions

Y.K., M.T., Z.X., and G.H. proposed and conceived the study. Z.X. conducted most of the data analysis and plotted all the figures. T.I., M.T., and Z.X. undertook MIROC6 experiments. Z.X., Y.K., and A.M. performed GFDL AM2.1 and LBM experiments. Z.X. led to writing the initial draft of the paper. Y.K. improved this manuscript in consultation with Z.X. All authors participated in interpreting and revising the paper.

Competing interests

The authors declare no competing interests.

Additional information

Supplementary information The online version contains supplementary material available at https://doi.org/10.1038/s41612-024-00864-2.

Correspondence and requests for materials should be addressed to Yu Kosaka or Gang Huang.